Prepared for submission to JHEP

Belle II Preprint 2025-xxx
KEK Preprint 2025-xxx

# Measurements of the branching fractions of $\Xi_c^+ \to \Sigma^+ K_S^0$, $\Xi_c^+ \to \Xi^0 \pi^+$, and $\Xi_c^+ \to \Xi^0 K^+$ at Belle and Belle II

## The Belle and Belle II Collaborations

**Email:** *coll-publications@belle2.org*

Abstract: Using data samples of 983 fb$^{-1}$ and 427.9 fb$^{-1}$ collected with the Belle and Belle II detectors at the KEKB and SuperKEKB asymmetric energy $e^+e^-$ colliders, respectively, we present studies of the Cabibbo-favored $\Xi_c^+$ decays $\Xi_c^+ \to \Sigma^+ K_S^0$ and $\Xi_c^+ \to \Xi^0\pi^+$, and the singly Cabibbo-suppressed decay $\Xi_c^+ \to \Xi^0 K^+$. We measure the ratios of branching fraction $\mathcal{B}(\Xi_c^+ \to \Sigma^+ K_S^0)/\mathcal{B}(\Xi_c^+ \to \Xi^-\pi^+\pi^+) = 0.064 \pm 0.007 \pm 0.003$ and $\mathcal{B}(\Xi_c^+ \to \Xi^0 K^+)/\mathcal{B}(\Xi_c^+ \to \Xi^-\pi^+\pi^+) = 0.016 \pm 0.002 \pm 0.001$ for the first time, and measure the branching fraction ratio $\mathcal{B}(\Xi_c^+ \to \Xi^0\pi^+)/\mathcal{B}(\Xi_c^+ \to \Xi^-\pi^+\pi^+) = 0.233 \pm 0.008 \pm 0.010$ with improved precision. The ratio of $\mathcal{B}(\Xi_c^+ \to \Xi^0\pi^+)$ and $\mathcal{B}(\Xi_c^+ \to \Xi^0 K^+)$ is measured to be $0.068 \pm 0.011 \pm 0.004$. Here, the first and second uncertainties are statistical and systematic, respectively. By multiplying the branching fraction of the normalization mode, $\mathcal{B}(\Xi_c^+ \to \Xi^-\pi^+\pi^+)$, we obtain the following absolute branching fractions

$$\begin{aligned}
\mathcal{B}(\Xi_c^+ \to \Sigma^+ K_S^0) &= (0.186 \pm 0.020 \pm 0.009 \pm 0.083)\%, \\
\mathcal{B}(\Xi_c^+ \to \Xi^0\pi^+) &= (0.677 \pm 0.024 \pm 0.030 \pm 0.303)\%, \\
\mathcal{B}(\Xi_c^+ \to \Xi^0 K^+) &= (0.046 \pm 0.007 \pm 0.002 \pm 0.021)\%,
\end{aligned}$$

where the third uncertainties are from $\mathcal{B}(\Xi_c^+ \to \Xi^-\pi^+\pi^+)$.

Keywords: $e^+e^-$ collider, Belle (II), Charmed baryon, Cabibbo-favored decay, Singly Cabibbo-suppressed decay

## Contents



## 1 Introduction

Charmed baryons offer a unique dynamical system to explore the intricate interplay between strong and weak interactions. Non-factorizable amplitudes arising from internal $W$-emission and $W$-exchange quark-level processes play a pivotal role, introducing significant challenges for the theoretical predictions in hadronic weak decays of charmed baryons [1]. Extensive efforts have been devoted to studying charmed baryon decays, aiming to develop a theoretical model for calculating non-factorizable contributions. Experimentally measuring the branching fractions of charmed baryons is indispensable for theoretical analysis.

In recent years, a number of experimental measurements of the branching fractions for $\Lambda_c^+$ and $\Xi_c^0$ decays have been reported [2, 3] since the absolute branching fractions of the antitriplet charmed baryons ($\Lambda_c^+$, $\Xi_c^{0,+}$) are now available [4–7]. These measurements inspired renewed theoretical research in the field of charmed baryons [1]. However, only a few other $\Xi_c^+$ decays have been measured [7, 8] since Belle reported the absolute branching fraction of $\Xi_c^+ \to \Xi^-\pi^+\pi^+$ [7]. Theoretical calculations for the two-body hadronic weak decays of $\Xi_c^+$ have been performed using the dynamical model [9] and $\mathrm{SU(3)_F}$ symmetry methods [10–16]. There are now predictions for a large number of the $\Xi_c^+$ Cabibbo-favored (CF) and the singly Cabibbo-suppressed (SCS) decay modes. It is worth noting that the CF decay $\Xi_c^+ \to \Sigma^+ K_S^0$ has not yet been measured, despite its predicted branching fraction being around $10^{-2}$ [9–16] suggesting that it should now be observable. Therefore, we study $\Xi_c^+ \to \Sigma^+ K_S^0$ for the first time. For another CF decay $\Xi_c^+ \to \Xi^0\pi^+$, the current measurement of the branching fraction has a considerable uncertainty [17]. We expect a more precise result based on the Belle and Belle II data. Meanwhile, the branching fraction of the SCS decay $\Xi_c^+ \to \Xi^0 K^+$ is predicted by different theoretical models to be in the

range $10^{-3}$ to $10^{-2}$ [9–16]. Since it is experimentally similar to $\Xi_c^+ \to \Xi^0\pi^+$, we search for it for the first time in Belle and Belle II data samples.

Here, we present the first measurement of the branching fractions for $\Xi_c^+ \to \Sigma^+ K_S^0$ and $\Xi_c^+ \to \Xi^0 K^+$ decays and an improved measurement of the branching fraction of $\Xi_c^+ \to \Xi^0\pi^+$. The $\Xi_c^+ \to \Xi^-\pi^+\pi^+$ decay is taken as the normalization mode for these measurements. This analysis uses data samples with integrated luminosities of 983 fb$^{-1}$ [18] and 427.9 fb$^{-1}$ [19] collected with the Belle and Belle II detectors operating at the KEKB and SuperKEKB asymmetric-energy $e^+e^-$ colliders, respectively. Charge-conjugate modes are implied throughout the paper.

## 2 Belle and Belle II experiments

The Belle detector [20, 21] operated from 1999 to 2010 at the KEKB asymmetric-energy $e^+e^-$ collider [22, 23]. Belle was a large cylindrical solid-angle magnetic spectrometer that consisted of a silicon vertex detector, a central drift chamber, an array of aerogel threshold Cherenkov counters, a barrel-like arrangement of time-of-flight scintillation counters, an electromagnetic calorimeter (ECL) comprised of CsI(Tl) crystals located inside a superconducting solenoid coil that provided a 1.5 T axial magnetic field, and an iron flux return placed outside the coil, instrumented with resistive-plate chambers to detect $K_L^0$ mesons and to identify muons. A detailed description of the detector can be found in refs. [20, 21].

The Belle II detector [24] is located at the interaction point (IP) of the SuperKEKB asymmetric-energy $e^+e^-$ collider [25]. Belle II is an upgraded version of the Belle detector and consists of several new subsystems and substantial upgrades to others. The new vertex detector includes two inner layers of pixel sensors and four outer layers of double-sided silicon micro-strip sensors. For the data sample used in this analysis, the second-pixel layer was incomplete, covering only one-sixth of the azimuthal angle. A new central drift chamber surrounding the vertex detector is used to measure the momenta and electric charges of charged particles. A time-of-propagation detector in the barrel and an aerogel ring-imaging Cherenkov detector in the forward endcap provide information for the identification of charged particles, supplemented by ionization energy loss measurements in the central drift chamber. The ECL readout electronics have been upgraded to cope with the higher beam-induced background environment at Belle II. The superconducting solenoid coil and the iron flux return for Belle are reused in Belle II, with the inner two layers of the barrel and the endcap resistive plate chambers of the $K_L^0$−muon detector replaced by plastic scintillator modules. The $z$ axis of the cylindrical laboratory frame is defined as the central solenoid axis with the positive direction toward the $e^-$ beam, common to Belle and Belle II.

## 3 Data samples

This measurement uses data recorded at center-of-mass (c.m.) energies at or near the $\Upsilon(1S)$, $\Upsilon(2S)$, $\Upsilon(3S)$, $\Upsilon(4S)$, and $\Upsilon(5S)$ resonances by the Belle detector, and at or near the $\Upsilon(4S)$ and at 10.75 GeV by the Belle II detector. The data samples correspond to integrated luminosities of 983 fb$^{-1}$ [18] and 427.9 fb$^{-1}$ [19] for Belle and Belle II, respectively.

Monte Carlo (MC) samples of simulated events are used to optimize the $\Xi_c^+$ candidate selection criteria, determine the reconstruction efficiency, and investigate any possible peaking background. Signal events are generated using the PYTHIA [26, 27] and EVTGEN [28] software packages via $e^+e^- \to c\bar{c}$, where one of the charm quarks is required to hadronize into a $\Xi_c^+$ baryon. Simulated $\Xi_c^0 \to \Sigma^+ K_S^0/\Xi^0\pi^+/\Xi^0 K^+/\Xi^-\pi^+\pi^+$ decays are generated with a phase space model. Background samples of $\Upsilon(4S) \to B^+B^-$ and $B^0\bar{B}^0$ decays at Belle and Belle II, as well as $\Upsilon(5S) \to B_s^{(*)0}\bar{B}_s^{(*)0}$ decays at Belle, are generated using EVTGEN and PYTHIA. The continuum background from $e^+e^- \to q\bar{q}$ processes, where $q$ indicates a $u$, $d$, $c$, or $s$ quark, is generated by the KKMC [29] software package, with PYTHIA used for hadronization and EVTGEN for subsequent decays of hadrons. Final state radiation effects are accounted for using the PHOTOS package [30]. Simulation of the detector response uses the GEANT3 [31] and GEANT4 [32] software packages for Belle and Belle II, respectively.

## 4 Selection criteria

We reconstruct the decays $\Xi_c^+ \to \Sigma^+ K_S^0$, $\Xi^0\pi^+$, $\Xi^0 K^+$, and $\Xi^-\pi^+\pi^+$, followed by the decays $\Xi^0 \to \Lambda\pi^0$, $\Xi^- \to \Lambda\pi^-$, $\Lambda \to p\pi^-$, $\Sigma^+ \to p\pi^0$, and $K_S^0 \to \pi^+\pi^-$. The Belle II software [33] is used for reconstructing data of both experiments, taking advantage of software improvements in Belle II. The Belle data is converted to the Belle II data format using the B2BII software package [34]. To improve the sensitivity for signal candidates, the selection criteria described below are optimized by maximizing the figure-of-merit, defined as $N_{\rm sig}/\sqrt{N_{\rm sig}+N_{\rm bkg}}$. Here, $N_{\rm sig}$ is the expected signal yield based on a theoretical prediction and a previous measurement of the branching fractions [2, 9], and $N_{\rm bkg}$ is the background yield determined from the inclusive MC samples in the $\Xi_c^+$ signal region: $|M(\Sigma^+K_S^0) - m_{\Xi_c^+}| < 30$ MeV/$c^2$, $|M(\Xi^0\pi^+) - m_{\Xi_c^+}| < 20$ MeV/$c^2$, and $|M(\Xi^0K^+) - m_{\Xi_c^+}| < 20$ MeV/$c^2$, where $m_i$ denotes the nominal mass of the particle $i$ [2] and $M(jk)$ indicates the invariant mass of the particles $j$ and $k$. The ranges of the $\Xi_c^+$ signal region are approximately three times the mass resolution ($\sim 3\sigma$), where $\sigma$ denotes the corresponding particle's mass resolution.

The impact parameters of charged tracks, except for those originating from decays of long-lived $K_S^0$ and hyperons ($\Xi^-$, $\Sigma^+$, and $\Lambda$), which are the distances of the closest approach of the reconstructed trajectory perpendicular to and along the z-axis to the calibrated IP region, are required to be less than 1.0 cm and 3.0 cm, respectively. These impact parameter requirements help suppress misreconstructed tracks and beam backgrounds. The identification of charged tracks is achieved by the likelihood ratio $\mathcal{R}(h|h') = \mathcal{L}(h)/(\mathcal{L}(h) + \mathcal{L}(h'))$, where $\mathcal{L}(h^{(\prime)})$ represents the likelihood of the charged track being a hadron ($h = \pi$, $K$, or $p$). The likelihood is determined using the Particle Identification (PID) algorithm, which integrates information from the Belle or Belle II subdetectors [35]. For pions, we require $\mathcal{R}(\pi|K) > 0.6$ and $\mathcal{R}(\pi|p) > 0.6$; for kaons, we require $\mathcal{R}(K|\pi) > 0.6$ and $\mathcal{R}(K|p) > 0.6$. These PID requirements have reconstruction efficiencies in the range 88%–92%. To suppress backgrounds from low-momentum pions and kaons, we require the momentum in the laboratory frame of pions and kaons to be greater than 0.5 GeV/$c$ for $\Xi_c^+ \to \Xi^0\pi^+$ and $\Xi_c^+ \to \Xi^0 K^+$, respectively.

The reconstruction and selection of $\Xi^-$ and $\Xi^0$ candidates are the same as those in refs. [36–39]. The $\Lambda$ candidates are reconstructed via the $\Lambda \to p\pi^-$ decay. The signal region of $\Lambda$ candidates is defined as $|M(p\pi^-) - m_\Lambda| < 3.5$ MeV/$c^2$ ($\sim 3\sigma$). Each $\pi^-$ candidate from the $\Xi^-$ decay is required to have a transverse momentum greater than 0.1 GeV/$c$ to remove backgrounds from low-momentum pions. Candidate $\pi^0$'s from $\Xi^0$ decays are reconstructed from pairs of photons selected from energy deposits in the ECL. To suppress low-momentum and fake photons, each photon candidate is required to have an energy greater than 30 MeV in the ECL barrel region ($-0.63 < \cos\theta < 0.85$); 50 (80) MeV for Belle (Belle II) in the forward endcap ($0.85 < \cos\theta < 0.98$); and 50 (60) MeV in the backward endcap ($-0.91 < \cos\theta < -0.63$), where $\theta$ is the polar angle in the laboratory frame. The signal region of the $\pi^0$ candidates is defined as $|M(\gamma\gamma) - m_{\pi^0}| < 11.6$ MeV/$c^2$ ($\sim 2\sigma$). In addition, the momenta of the $\pi^0$ candidates in the laboratory frame are required to exceed 0.25 GeV/$c$. Finally, $\Xi^-$ and $\Xi^0$ candidates are formed from $\Lambda\pi^-$ and $\Lambda\pi^0$ combinations, respectively. A vertex fit is performed to the entire $\Xi^{-(0)}$ decay chain, including subsequent decay products, with the $p\pi$ and diphoton masses constrained to match the known $\Lambda$ and $\pi^0$ masses [2]. The signal regions of $\Xi^-$ and $\Xi^0$ candidates are defined as $|M(\Lambda\pi^-) - m_{\Xi^-}| < 6.6$ MeV/$c^2$ ($\sim 3\sigma$) and $|M(\Lambda\pi^0) - m_{\Xi^0}| < 6.0$ MeV/$c^2$ ($\sim 2\sigma$), respectively.

The $K^0_S$ candidates decaying to $\pi^+\pi^-$ are selected with an artificial neural network [40]. For Belle II, the flight distance of each $K^0_S$ is required to be larger than 0.5 cm to remove random combinations of pions. Here, the flight distance of $K^0_S$ is calculated as the projection of the displacement vector, which joins its production and decay vertices, onto the direction of its momentum. The signal region of $K^0_S$ invariant mass is defined as $|M(\pi^+\pi^-) - m_{K^0_S}| < 7.0$ MeV/$c^2$ ($\sim 2\sigma$). The $\Sigma^+$ candidates are reconstructed in the $\Sigma^+ \to p\pi^0$ decay mode, with the likelihood ratio requirements $\mathcal{R}(p|\pi) > 0.6$ and $\mathcal{R}(p|K) > 0.6$ for the proton candidates. The distance of the closest approach of the proton to the IP in the transverse plane is greater than 0.1 cm. For $\pi^0$ candidates, each $\pi^0$ is reconstructed from two photons. The same requirements used for $\Xi^0$ candidates for the photon energy are applied. To reduce the combinatorial backgrounds, the $\pi^0$ momentum in the c.m. frame must be greater than 0.45 GeV/$c$. A vertex fit is applied to the entire $\Sigma^+$ decay chain, with the $\pi^0$ invariant mass constrained. The reconstructed $\Sigma^+$ satisfies the requirement $\cos\alpha > 0.0$, where $\alpha$ is the angle between the momentum and the vertex vector of $\Sigma^+$, where the vertex vector connecting the IP and fitted vertex. The efficiency loss for this selection is less than 1%. For selected $\Sigma^+$ candidates, $|M(p\pi^0) - m_{\Sigma^+}| < 7.0$ MeV/$c^2$ ($\sim 1.5\sigma$) is required.

The $\Xi_c^+$ candidates are reconstructed from $\Xi^-\pi^+\pi^+$, $\Sigma^+K^0_S$, $\Xi^0\pi^+$, and $\Xi^0K^+$. A global decay chain vertex fit is applied for each mode using the TreeFit algorithm with mass constraints for the intermediate states and ensuring that the $\Xi_c^+$ originates from the interaction region [41]. To suppress backgrounds, especially those from $B$-meson decays, we require the scaled momentum $x_p = p^*_{\Xi_c^+}/p_{\rm max}$ to be larger than 0.55 in both Belle and Belle II. Here, the $p^*_{\Xi_c^+}$ is the momentum of the $\Xi_c^+$ candidates in the c.m. frame, and $p_{\rm max}$ $= \frac{1}{\rm c}\sqrt{E^2_{\rm beam} - M^2_{\Xi_c^+}{\rm c}^4}$, where the $E_{\rm beam}$ is the beam energy in the c.m. frame and $M_{\Xi_c^+}$ is the invariant mass of $\Xi_c^+$ candidates.

## 5 Measurements of the branching fractions

The $\Xi^-\pi^+\pi^+$ invariant mass distributions for $\Xi_c^+$ candidates in Belle and Belle II data are shown in the figure 1 after applying all event selection criteria, together with the results of an unbinned extended maximum-likelihood (EML) fit. A sum of two Gaussians is used as the signal probability density function (PDF) for the $\Xi_c^+$ shape, while the background is represented by a first-order polynomial. All signal and background parameters are allowed to float in the fit. The pulls $(N_{\rm data} - N_{\rm fit})/\sigma_{\rm data}$ are displayed in figure 1, where $N_{\rm data}$ is the number of entries in each bin from data, $N_{\rm fit}$ is the fit result in each bin, and $\sigma_{\rm data}$ is the uncertainty on $N_{\rm data}$. The fitted signal yields are summarized in table 1.

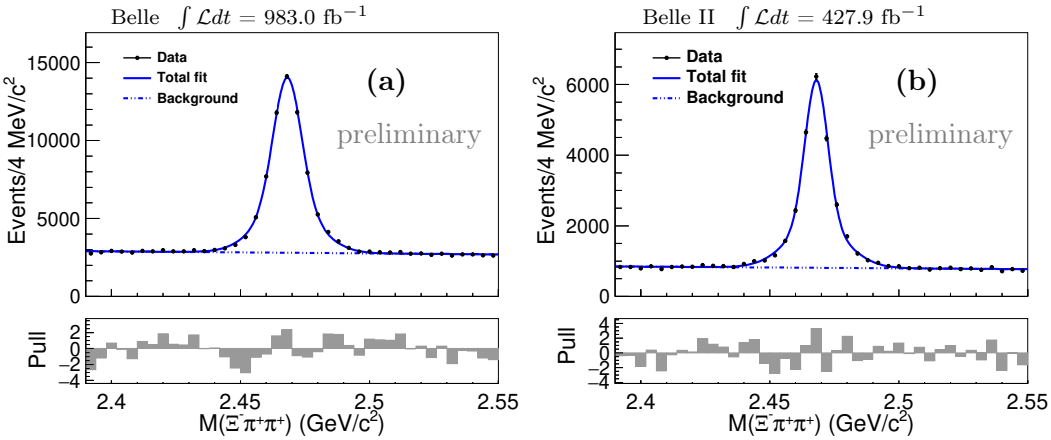


**Figure 1**. Invariant mass distributions of $\Xi^-\pi^+\pi^+$ from (a) Belle and (b) Belle II data. The markers with error bars represent the data, the solid blue curves show the fit results, and the dashed blue curves show the background component of the fit.

Figure 2 shows the Dalitz distributions of $M^2(\Xi^-\pi_L^+)$ versus $M^2(\Xi^-\pi_H^+)$ in $\Xi_c^+$ signal region after subtracting the normalized events from $\Xi_c^+$ sideband regions, where the $\Xi^-\pi^+$ combination with a higher (lower) invariant mass is labeled as $M^2(\Xi^-\pi_H^+)$ ($M^2(\Xi^-\pi_L^+)$). Here, the $\Xi_c^+$ signal and sideband regions for $\Xi_c^+ \to \Xi^-\pi^+\pi^+$ mode are defined as $|M_{\Xi^-\pi^+\pi^+} - m_{\Xi_c^+}| < 24$ MeV/$c^2$ ($\sim 3\sigma$) and $|M_{\Xi^-\pi^+\pi^+} - m_{\Xi_c^+}| \in [40, 64]$ MeV/$c^2$, respectively. We divide the Dalitz plot into $20 \times 30$ bins and then apply a bin-by-bin correction for the efficiency. The reconstruction efficiency averaged over the Dalitz plot is determined via the formula

$$\varepsilon^{\rm corr} = \frac{\sum_i N_i}{\sum_i (N_i/\varepsilon_i)}, \tag{5.1}$$

where $i$ is summed over all bins; the reconstruction efficiency of each Dalitz plot bin ($\varepsilon_i$) is obtained from MC simulation. Here, $N_i$ is the number of signal candidates for the $i^{\rm th}$ bin in data calculated as $N_i = N_i^{\rm tot} - N_b^{\rm SR} f_i^b$. Here $N_i^{\rm tot}$ is the yield in the $i^{\rm th}$ bin of the Dalitz distribution in the $\Xi_c^+$ signal region, $N_b^{\rm SR}$ is the fitted background yield in the $\Xi_c^+$ signal region in data, and $f_i^b$ is the fraction of background in the $i^{\rm th}$ bin, with $\sum_i f_i^b = 1$. After Dalitz corrections, the signal efficiencies $\varepsilon_{\Xi^-\pi^+\pi^+}$ are determined to be $(11.37 \pm 0.04)\%$ and $(10.98 \pm 0.03)\%$ for Belle and Belle II, respectively, and are listed in table 1.

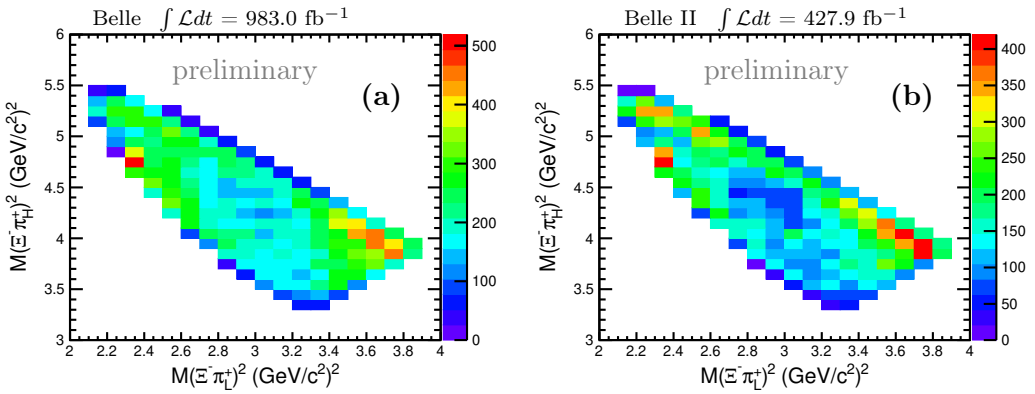


**Figure 2**. Dalitz distributions of the reconstructed $\Xi^-\pi^+\pi^+$ candidates from (a) Belle and (b) Belle II data in the $\Xi_c^+$ signal region with the normalized $\Xi_c^+$ sideband events subtracted.

Distributions of $M(\Sigma^+K_S^0)$, $M(\Xi^0\pi^+)$, and $M(\Xi^0K^+)$ of $\Xi_c^+$ candidates reconstructed in data are shown in figure 3. These invariant mass distributions are used to extract $\Xi_c^+$ signal yields from an unbinned EML fit. We study the backgrounds of $M(\Sigma^+K_S^0)$, $M(\Xi^0\pi^+)$, and $M(\Xi^0K^+)$ using simulation [42] and $\Sigma^+/\Xi^0$ data sidebands, respectively. In addition to a flat combinatorial component, there is a peaking background component, referred to as broken-signal, dominated by random photons not associated with the signal decay, which is described by a non-parametric kernel estimation PDF [43] ($\mathcal{F}_{\rm broken}$) obtained from MC simulation. The total fit PDF includes, therefore, terms for the signal ($\mathcal{F}_{\rm sig}$), $\mathcal{F}_{\rm broken}$, and smooth background ($\mathcal{F}_{\rm bkg}$) contributions:

$$\mathcal{F} = n_{\rm sig}\mathcal{F}_{\rm sig} + n_{\rm broken}\mathcal{F}_{\rm broken} + n_{\rm bkg}\mathcal{F}_{\rm bkg}, \tag{5.2}$$

where $n_{\rm sig}$, $n_{\rm broken}$, and $n_{\rm bkg}$ are the numbers of $\Xi_c^+$ signal events, broken-signal events, and smooth background events, respectively. The values of $n_{\rm sig}$ and $n_{\rm bkg}$ are free in the fit, while the ratios of $n_{\rm broken}$ to $n_{\rm sig}$ are fixed to the fractions from MC simulations and are 15.4% (15.9%), 19.4% (18.4%), and 18.0% (18.5%) for the $\Xi_c^+ \to \Sigma^+K_S^0$, $\Xi_c^+ \to \Xi^0\pi^+$, and $\Xi_c^0 \to \Xi^0K^+$ decay modes, respectively, at Belle (Belle II). The signal shapes of $\Xi_c^+$ candidates are modeled using the sum of two Gaussians with a common mean, where the fractions and parameters are obtained from the corresponding MC simulation, except for the $\Xi_c^+ \to \Xi^0\pi^+$ mode. The $\mathcal{F}_{\rm bkg}$ contribution is parameterized by a second-order polynomial for each mode. All the parameters for $\mathcal{F}_{\rm bkg}$ are free in the fit. A validation of the fit through MC simulation confirms that the results are unbiased and the uncertainties follow a Gaussian distribution. The reconstruction efficiencies and fit results for each mode are listed in table 1. The reconstruction efficiencies for each mode in Belle II are larger than those in Belle due to improved photon reconstruction stemming from timing improvements in the ECL readout electronics. The statistical significances for $\Xi_c^+ \to \Sigma^+K_S^0$, $\Xi_c^+ \to \Xi^0\pi^+$, and $\Xi_c^+ \to \Xi^0K^+$ are $7.4\sigma$ ($5.7\sigma$), $>10\sigma$ ($>10\sigma$), and $4.7\sigma$ ($5.4\sigma$) in Belle (Belle II), respectively, estimated using $-2\ln(\mathcal{L}_0/\mathcal{L}_{\rm max})$ from the difference of the logarithmic likelihoods [44], where $\mathcal{L}_0$ and $\mathcal{L}_{\rm max}$ are the values of the likelihood without and with the signal component, respectively. The difference in the number of degrees of freedom in the fit

| Mode | Belle yield | $\varepsilon_{\text{Belle}}$ (%) | Belle II yield | $\varepsilon_{\text{Belle II}}$ (%) |
|---|---|---|---|---|
| $\Xi_c^+ \to \Xi^-\pi^+\pi^+$ | $(487 \pm 4) \times 10^2$ | $11.37 \pm 0.04$ | $(196 \pm 2) \times 10^2$ | $10.98 \pm 0.03$ |
| $\Xi_c^+ \to \Sigma^+ K_S^0$ | $286 \pm 40$ | $1.95 \pm 0.03$ | $178 \pm 31$ | $2.83 \pm 0.02$ |
| $\Xi_c^+ \to \Xi^0\pi^+$ | $2728 \pm 165$ | $2.79 \pm 0.04$ | $1419 \pm 63$ | $3.45 \pm 0.03$ |
| $\Xi_c^+ \to \Xi^0 K^+$ | $134 \pm 30$ | $2.15 \pm 0.03$ | $94 \pm 19$ | $3.14 \pm 0.03$ |

**Table 1**. Observed $\Xi_c^+$ signal yields and reconstruction efficiencies for the studied modes. Uncertainties are statistical only.

are 1 for $\Xi_c^+ \to \Sigma^+ K_S^0$ and $\Xi_c^+ \to \Xi^0 K^+$ modes, and 4 for $\Xi_c^+ \to \Xi^0\pi^+$, and are taken into account to estimate the statistical significance. Alternative fits to the $\Xi^0 K^+$ mass spectra are performed: (1) changing the fit range by 10%, (2) changing the order of polynomial for the smooth background, (3) floating the ratio of $n_{\text{broken}}$ to $n_{\text{sig}}$. The significance for $\Xi_c^+ \to \Xi^0 K^+$ mode is larger than $4.5\sigma$ and $5.1\sigma$ for Belle and Belle II, respectively, in all cases.

The ratios of branching fractions to the normalization mode $\Xi_c^+ \to \Xi^-\pi^+\pi^+$ are calculated via

$$\begin{aligned}
\frac{\mathcal{B}(\Xi_c^+ \to \Sigma^+ K_S^0)}{\mathcal{B}(\Xi_c^+ \to \Xi^-\pi^+\pi^+)} &= \frac{N_{\Sigma^+ K_S^0}\varepsilon_{\Xi^-\pi^+\pi^+}}{\varepsilon_{\Sigma^+ K_S^0} N_{\Xi^-\pi^+\pi^+}} \times \frac{\mathcal{B}(\Xi^- \to \Lambda\pi^-)\mathcal{B}(\Lambda \to p\pi^-)}{\mathcal{B}(\Sigma^+ \to p\pi^0)\mathcal{B}(K_S^0 \to \pi^+\pi^-)\mathcal{B}(\pi^0 \to \gamma\gamma)}, \\
\frac{\mathcal{B}(\Xi_c^+ \to \Xi^0\pi^+)}{\mathcal{B}(\Xi_c^+ \to \Xi^-\pi^+\pi^+)} &= \frac{N_{\Xi^0\pi^+}\varepsilon_{\Xi^-\pi^+\pi^+}}{\varepsilon_{\Xi^0\pi^+} N_{\Xi^-\pi^+\pi^+}} \times \frac{\mathcal{B}(\Xi^- \to \Lambda\pi^-)}{\mathcal{B}(\Xi^0 \to \Lambda\pi^0)\mathcal{B}(\pi^0 \to \gamma\gamma)}, \\
\frac{\mathcal{B}(\Xi_c^+ \to \Xi^0 K^+)}{\mathcal{B}(\Xi_c^+ \to \Xi^-\pi^+\pi^+)} &= \frac{N_{\Xi^0 K^+}\varepsilon_{\Xi^-\pi^+\pi^+}}{\varepsilon_{\Xi^0 K^+} N_{\Xi^-\pi^+\pi^+}} \times \frac{\mathcal{B}(\Xi^- \to \Lambda\pi^-)}{\mathcal{B}(\Xi^0 \to \Lambda\pi^0)\mathcal{B}(\pi^0 \to \gamma\gamma)}.
\end{aligned} \tag{5.3}$$

Here, $N_{\Sigma^+ K_S^0}$, $N_{\Xi^0\pi^+}$, $N_{\Xi^0 K^+}$, and $N_{\Xi^-\pi^+\pi^+}$ are the $\Xi_c^+$ yields resulting from the fits; $\varepsilon_{\Sigma^+ K_S^0}$, $\varepsilon_{\Xi^0\pi^+}$, $\varepsilon_{\Xi^0 K^+}$, and $\varepsilon_{\Xi^-\pi^+\pi^+}$ are the corresponding reconstruction efficiencies; and the branching fractions are taken from ref. [2]. Meanwhile, the branching branching ratio of $\mathcal{B}(\Xi_c^+ \to \Xi^0 K^+)/\mathcal{B}(\Xi_c^+ \to \Xi^0\pi^+)$ is calculated by

$$\frac{\mathcal{B}(\Xi_c^+ \to \Xi^0 K^+)}{\mathcal{B}(\Xi_c^+ \to \Xi^0\pi^+)} = \frac{N_{\Xi^0 K^+}\varepsilon_{\Xi^0\pi^+}}{\varepsilon_{\Xi^0 K^+} N_{\Xi^0\pi^+}}. \tag{5.4}$$

We combine the Belle and Belle II branching fraction ratios and uncertainties using the formulas in ref. [45],

$$\begin{aligned}
r &= \frac{r_1\sigma_2^2 + r_2\sigma_1^2}{\sigma_1^2 + \sigma_2^2 + (r_1 - r_2)^2\epsilon_r^2}, \\
\sigma &= \sqrt{\frac{\sigma_1^2\sigma_2^2 + (r_1^2\sigma_2^2 + r_2^2\sigma_1^2)\epsilon_r^2}{\sigma_1^2 + \sigma_2^2 + (r_1 - r_2)^2\epsilon_r^2}},
\end{aligned} \tag{5.5}$$

where $r_i$, $\sigma_i$, and $\epsilon_r$ are the branching fraction ratio, uncorrelated uncertainty, and relative correlated systematic uncertainty from each data sample, respectively. The branching fraction ratios are summarized in table 2, where the first uncertainty is statistical and the second systematic. The systematic uncertainties are discussed in the Section 6.

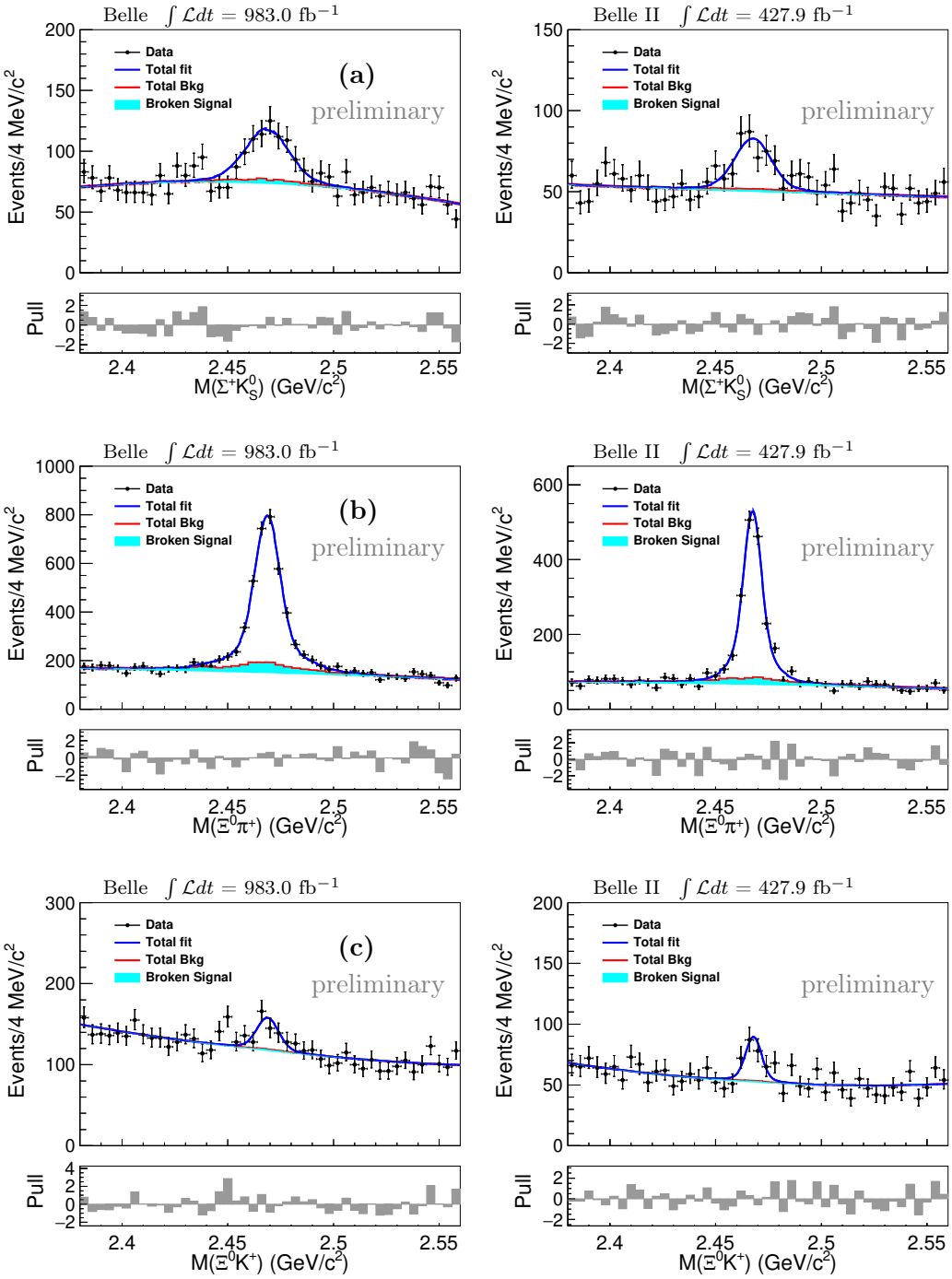


**Figure 3**. Invariant mass distributions of $\Xi_c^+$ candidates from (a) $\Xi_c^+ \to \Sigma^+ K_S^0$, (b) $\Xi_c^+ \to \Xi^0\pi^+$, and (c) $\Xi_c^+ \to \Xi^0 K^+$ decays reconstructed in (left) Belle and (right) Belle II data. The black dots with error bars show the distribution from the data. The solid blue curves and red curves show the total fit and total backgrounds, respectively. The cyan areas show the broken-signal component.

| Mode | Belle | Belle II | Combined |
|---|---|---|---|
| $\mathcal{B}(\Xi_c^+ \to \Sigma^+ K_S^0)/\mathcal{B}(\Xi_c^+ \to \Xi^-\pi^+\pi^+)$ | $0.062 \pm 0.009 \pm 0.004$ | $0.067 \pm 0.012 \pm 0.005$ | $0.064 \pm 0.007 \pm 0.003$ |
| $\mathcal{B}(\Xi_c^+ \to \Xi^0\pi^+)/\mathcal{B}(\Xi_c^+ \to \Xi^-\pi^+\pi^+)$ | $0.232 \pm 0.014 \pm 0.013$ | $0.234 \pm 0.010 \pm 0.014$ | $0.233 \pm 0.008 \pm 0.010$ |
| $\mathcal{B}(\Xi_c^+ \to \Xi^0 K^+)/\mathcal{B}(\Xi_c^+ \to \Xi^-\pi^+\pi^+)$ | $0.015 \pm 0.003 \pm 0.001$ | $0.017 \pm 0.003 \pm 0.001$ | $0.016 \pm 0.002 \pm 0.001$ |
| $\mathcal{B}(\Xi_c^+ \to \Xi^0 K^+)/\mathcal{B}(\Xi_c^+ \to \Xi^0\pi^+)$ | $0.064 \pm 0.015 \pm 0.005$ | $0.073 \pm 0.015 \pm 0.006$ | $0.068 \pm 0.011 \pm 0.004$ |

**Table 2**. Branching fraction ratios of $\Xi_c^+ \to \Sigma^+ K_S^0$, $\Xi^0\pi^+$, and $\Xi^0 K^+$ decays relative to $\Xi_c^+ \to \Xi^-\pi^+\pi^+$ and the ratio of $\mathcal{B}(\Xi_c^+ \to \Xi^0 K^+)$ and $\mathcal{B}(\Xi_c^+ \to \Xi^0\pi^+)$. The first uncertainty is statistical and the second systematic.

## 6 Systematic uncertainties

There are several sources of systematic uncertainties in the measurements of the branching fraction ratios, including those associated with efficiency, the branching fraction of the intermediate state, and the fit procedure. Note that the uncertainties from efficiency-related sources and the branching fraction of the intermediate state partially cancel when taking the ratio to the normalization mode. Table 3 summarizes the systematic uncertainties, with the total uncertainty calculated as the quadratic sum of the uncertainties from each source. For the branching fraction ratio $\mathcal{B}(\Xi_c^+ \to \Xi^0 K^+)/\mathcal{B}(\Xi_c^+ \to \Xi^0\pi^+)$, the uncertainties related to $\Xi^0$ reconstruction and $\pi^+/K^+$ tracking cancel, so that the remaining uncertainties come from detection efficiency-related sources (PID and MC statistic) and the fit procedure (broken-signal ratio, fit range, and background shape).

The detection efficiencies determined from simulations are corrected by multiplicative data-to-simulation ratios determined from data control samples, and the uncertainties on the correction factors are taken as systematic uncertainties. The correction factors and uncertainties include those from track-finding efficiency, obtained from the control samples of $D^{*+} \to D^0(\to K_S^0\pi^+\pi^-)\pi^+$ at Belle and $\overline{B}^0 \to D^{*+}(\to D^0\pi^+)\pi^-$ and $e^+e^- \to \tau^+\tau^-$ at Belle II. At Belle, the PID uncertainties for charged pion, kaon, and proton are studied using $D^{*+} \to D^0(\to K^-\pi^+)\pi^+$ and $\Lambda \to p\pi^-$ [35] control samples, respectively. At Belle II, the PID uncertainties are obtained using $K_S^0 \to \pi^-\pi^+$ and $\Lambda \to p\pi^-$ [46] control samples, respectively. The uncertainties of $\pi^0$ reconstruction are obtained from the $\tau \to \pi^-\pi^0\nu_\tau$ control sample at Belle and the $D^0 \to K^-\pi^+\pi^0$ control sample at Belle II. The uncertainty associated with the mass windows of $\pi^0$ is calculated by the data-simulation difference on the fraction of the fitted $\pi^0$ signal yield in the $\pi^0$ signal region over that in the total region. This uncertainty is added in quadrature with $\pi^0$ reconstruction. The $K_S^0$ reconstruction uncertainties are obtained from the control samples of $D^{*+} \to D^0(\to K_S^0\pi^0)\pi^+$ at Belle and $D^{*+} \to D^0(\to K_S^0\pi^+\pi^-)\pi^+$ at Belle II. Since we applied a decay length selection for $K_S^0$ in the Belle II data, the uncertainty is calculated by the data-simulation difference on the fraction of the fitted $K_S^0$ signal yield in the $K_S^0$ signal region divided by that in the total region. This uncertainty is added in quadrature with the uncertainty in $K_S^0$ reconstruction. The uncertainties of $\Lambda$ reconstruction are obtained for the control samples of $\Lambda \to p\pi$ and $\Xi_c^+ \to \Xi^-\pi^+\pi^+$ at Belle and Belle II, respectively. The uncertainty due to the photon reconstruction is included in the uncertainty due to $\pi^0$ reconstruction. The uncertainties of the intermediate particle ($\Sigma^+$ and $\Xi^0$) signal regions selection are calculated from the

| Source | $\frac{\mathcal{B}(\Xi_c^+\to\Sigma^+K_S^0)}{\mathcal{B}(\Xi_c^+\to\Xi^-\pi^+\pi^+)}$ | | $\frac{\mathcal{B}(\Xi_c^+\to\Xi^0\pi^+)}{\mathcal{B}(\Xi_c^+\to\Xi^-\pi^+\pi^+)}$ | | $\frac{\mathcal{B}(\Xi_c^+\to\Xi^0K^+)}{\mathcal{B}(\Xi_c^+\to\Xi^-\pi^+\pi^+)}$ | |
|---|---|---|---|---|---|---|
| | Belle | Belle II | Belle | Belle II | Belle | Belle II |
| Tracking | 1.3 | 1.3 | 0.7 | 1.3 | 0.7 | 1.3 |
| PID | 0.1 | 0.2 | 0.1 | 0.1 | 0.1 | 0.2 |
| $\pi^0$ reconstruction | 2.2 | 4.2 | 2.4 | 2.3 | 2.3 | 2.3 |
| $K_S^0$ reconstruction | 0.8 | 2.3 | - | - | - | - |
| $\Lambda$ reconstruction | 0.5 | 0.7 | - | - | - | - |
| $\Sigma^+$ mass window | 1.4 | 1.6 | - | - | - | - |
| $\Xi^0$ mass window | - | - | 0.4 | 0.6 | 1.1 | 1.4 |
| MC statistic | 2.0 | 1.0 | 2.0 | 1.0 | 2.0 | 1.0 |
| Dalitz efficiency-correction | 3.0 | 2.9 | 3.0 | 2.9 | 3.0 | 2.9 |
| Broken-signal ratio | 3.5 | 4.5 | 2.3 | 3.5 | 3.7 | 3.2 |
| Fit range | 0.7 | 1.1 | 0.9 | 0.9 | 1.5 | 2.1 |
| Background shape | 1.5 | 1.5 | 2.4 | 2.4 | 2.2 | 2.2 |
| Intermediate states $\mathcal{B}$ | 1.0 | 1.0 | 0.1 | 0.1 | 0.1 | 0.1 |
| Total | 6.2 | 7.9 | 5.6 | 6.1 | 6.4 | 6.2 |

**Table 3**. Fractional systematic uncertainties (%) on the relative branching-fraction results. The uncertainties in the last two rows, due to intermediate branching fractions and background shape, are common to Belle and Belle II; the other uncertainties are independent. Since the $\Lambda \to p\pi^-$ decay is reconstructed in $\Xi_c^+ \to \Xi^0\pi^+$ and $\Xi_c^+ \to \Xi^0K^+$, the $\mathcal{B}(\Lambda \to p\pi^-)$ uncertainty and the uncertainty due to the $\Lambda \to p\pi^-$ reconstruction efficiency cancel in the ratios of $\frac{\mathcal{B}(\Xi_c^+\to\Xi^0\pi^+)}{\mathcal{B}(\Xi_c^+\to\Xi^-\pi^+\pi^+)}$ and $\frac{\mathcal{B}(\Xi_c^+\to\Xi^0K^+)}{\mathcal{B}(\Xi_c^+\to\Xi^-\pi^+\pi^+)}$.

data-simulation difference on the fraction of the $\Sigma^+$ and $\Xi^0$ signal yield in the $\Sigma^+$ and $\Xi^0$ signal region over that in the total signal region, respectively. The systematic uncertainty due to the limited MC simulation sample sizes is calculated using a binomial uncertainty estimate. For the reference mode $\Xi_c^+ \to \Xi^-\pi^+\pi^+$, the signal efficiency is corrected across the Dalitz plot. Since the selected $\Xi_c^+$ sideband regions may influence the efficiency, we shift the $\Xi_c^+$ sideband regions by $\pm 5$ MeV/$c^2$, and the average deviation in efficiency compared to the nominal value is taken as systematic uncertainty.

The uncertainties due to the fit procedure are determined by taking the differences between the $\Xi_c^+ \to \Sigma^+K_S^0$, $\Xi_c^+ \to \Xi^0\pi^+$, and $\Xi_c^+ \to \Xi^0K^+$ signal yields in the nominal fits and the signal yields in fits with the following modifications: (1) changing the fit range by 10%, (2) changing the order of polynomial for the smooth background, (3) floating the ratio of $n_{\rm broken}$ to $n_{\rm sig}$. The order of the polynomial for the background shape is the same for the two experiments, and the corresponding uncertainty is extracted from a simultaneous fit for the $\Xi_c^+$ signal yield in Belle and Belle II data. The total systematic uncertainty is obtained by adding the contributions from each source in quadrature. For the normalization mode $\Xi_c^+ \to \Xi^-\pi^+\pi^+$, the uncertainties are considered similarly by changing the fit range and the order of the background polynomial. These uncertainties are added in quadrature for the corresponding branching fraction ratio measurements.

The systematic uncertainties due to the intermediate branching fractions are taken to be the uncertainties on the world-average values [2] and treated as correlated uncertainties, which are common to Belle and Belle II. For the measurement of $\frac{\mathcal{B}(\Xi_c^+\to\Sigma^+K_S^0)}{\mathcal{B}(\Xi_c^+\to\Xi^-\pi^+\pi^+)}$, the uncertainties from $\mathcal{B}(\Sigma^+ \to p\pi^0)$, $\mathcal{B}(K_S^0 \to \pi^+\pi^-)$, $\mathcal{B}(\pi^0 \to \gamma\gamma)$, $\mathcal{B}(\Xi^- \to \Lambda\pi^-)$, and $\mathcal{B}(\Lambda \to p\pi^-)$ are 0.58%, 0.07%, 0.03%, 0.04%, and 0.78% [2], which are added in quadrature as the total uncertainty from branching fractions of intermediate states. For the measurements of $\frac{\mathcal{B}(\Xi_c^+\to\Xi^0\pi^+)}{\mathcal{B}(\Xi_c^+\to\Xi^-\pi^+\pi^+)}$ and $\frac{\mathcal{B}(\Xi_c^+\to\Xi^0K^+)}{\mathcal{B}(\Xi_c^+\to\Xi^-\pi^+\pi^+)}$, the uncertainties from $\mathcal{B}(\Xi^- \to \Lambda\pi^-)$, $\mathcal{B}(\Xi^0 \to \Lambda\pi^0)$, and $\mathcal{B}(\pi^0 \to \gamma\gamma)$ are 0.04%, 0.01%, and 0.03% [2], respectively. The 44.8% uncertainty on $\mathcal{B}(\Xi_c^+ \to \Xi^-\pi^+\pi^+)$ [7] is treated as an independent systematic uncertainty in the measurement of the absolute branching fractions.

Adding the contributions from each source in quadrature in table 3, the total systematic uncertainties are 6.1% (7.8%), 5.6% (6.2%), 6.4% (6.1%), and 5.1% (6.1%) for $\frac{\mathcal{B}(\Xi_c^+\to\Sigma^+K_S^0)}{\mathcal{B}(\Xi_c^+\to\Xi^-\pi^+\pi^+)}$, $\frac{\mathcal{B}(\Xi_c^+\to\Xi^0\pi^+)}{\mathcal{B}(\Xi_c^+\to\Xi^-\pi^+\pi^+)}$, $\frac{\mathcal{B}(\Xi_c^+\to\Xi^0K^+)}{\mathcal{B}(\Xi_c^+\to\Xi^-\pi^+\pi^+)}$, and $\frac{\mathcal{B}(\Xi_c^+\to\Xi^0K^+)}{\mathcal{B}(\Xi_c^+\to\Xi^0\pi^+)}$ at Belle (Belle II), respectively.

## 7 Summary and discussion

We present measurements of branching fractions of $\Xi_c^+$ decays into $\Sigma^+K_S^0$, $\Xi^0\pi^+$, and $\Xi^0K^+$ final states, using 983 fb$^{-1}$ and 427.9 fb$^{-1}$ of data samples collected by the Belle and Belle II experiments, respectively. The process $\Xi_c^+ \to \Xi^-\pi^+\pi^+$ is used as a reference mode. The branching fractions relative to $\mathcal{B}(\Xi_c^+ \to \Xi^-\pi^+\pi^+)$ are measured to be

$$\frac{\mathcal{B}(\Xi_c^+ \to \Sigma^+K_S^0)}{\mathcal{B}(\Xi_c^+ \to \Xi^-\pi^+\pi^+)} = 0.064 \pm 0.007(\text{stat.}) \pm 0.003(\text{syst.}), \tag{7.1}$$

$$\frac{\mathcal{B}(\Xi_c^+ \to \Xi^0\pi^+)}{\mathcal{B}(\Xi_c^+ \to \Xi^-\pi^+\pi^+)} = 0.233 \pm 0.008(\text{stat.}) \pm 0.010(\text{syst.}), \tag{7.2}$$

and

$$\frac{\mathcal{B}(\Xi_c^+ \to \Xi^0K^+)}{\mathcal{B}(\Xi_c^+ \to \Xi^-\pi^+\pi^+)} = 0.016 \pm 0.002(\text{stat.}) \pm 0.001(\text{syst.}), \tag{7.3}$$

where the first uncertainties are statistical and the second are systematic. The ratio of $\mathcal{B}(\Xi_c^+ \to \Xi^0K^+)/\mathcal{B}(\Xi_c^+ \to \Xi^0\pi^+)$ is measured to be $0.068 \pm 0.011(\text{stat.}) \pm 0.004(\text{syst.})$. Taking $\mathcal{B}(\Xi_c^+ \to \Xi^-\pi^+\pi^+) = (2.9\pm1.3)\%$ [2], the absolute branching fractions are measured to be

$$\mathcal{B}(\Xi_c^+ \to \Sigma^+K_S^0) = (0.186 \pm 0.020(\text{stat.}) \pm 0.009(\text{syst.}) \pm 0.083(\text{norm.}))\%, \tag{7.4}$$

$$\mathcal{B}(\Xi_c^+ \to \Xi^0\pi^+) = (0.677 \pm 0.024(\text{stat.}) \pm 0.030(\text{syst.}) \pm 0.303(\text{norm.}))\%, \tag{7.5}$$

and

$$\mathcal{B}(\Xi_c^+ \to \Xi^0K^+) = (0.046 \pm 0.007(\text{stat.}) \pm 0.002(\text{syst.}) \pm 0.021(\text{norm.}))\%, \tag{7.6}$$

where the third uncertainty is from $\mathcal{B}(\Xi_c^+ \to \Xi^-\pi^+\pi^+)$.

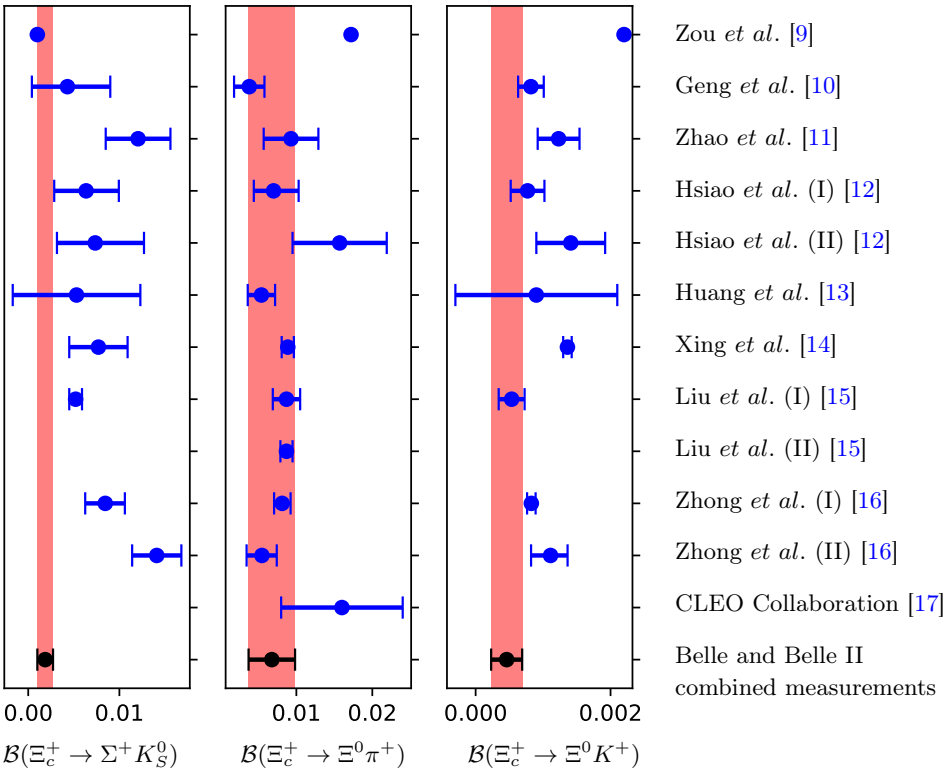


**Figure 4**. The comparisons of the measured $\mathcal{B}(\Xi_c^+ \to \Sigma^+ K_S^0)$, $\mathcal{B}(\Xi_c^+ \to \Xi^0 \pi^+)$, $\mathcal{B}(\Xi_c^+ \to \Xi^0 K^+)$ with theoretical predictions [9–16]. Dots with error bars represent central values and their uncertainties; those without indicate a lack of theoretical uncertainty. Missing dots signify the absence of theoretical predictions or experimental results for that decay mode. The black dots with error bars denote the results of this study. The red vertical bands cover a $1\sigma$ region corresponding to the measurements presented in this work.

Figure 4 shows the comparison of measurements of the branching fractions with theoretical calculations as mentioned in Section 1. Two predictions utilizing $\mathrm{SU(3)_F}$ symmetry with the IRA method [10, 13] align well with our measurements across all decay channels. Predictions for $\mathcal{B}(\Xi_c^+ \to \Sigma^+ K_S^0)$ in refs. [11, 15, 16], $\mathcal{B}(\Xi_c^+ \to \Xi^0 \pi^+)$ in refs [9], and $\mathcal{B}(\Xi_c^+ \to \Xi^0 K^+)$ in refs [9, 14] deviate from our measurements by more than $2\sigma$.

## Acknowledgments

This work, based on data collected using the Belle II detector, which was built and commissioned prior to March 2019, and data collected using the Belle detector, which was operated until June 2010, was supported by Higher Education and Science Committee of the Republic of Armenia Grant No. 23LCG-1C011; Australian Research Council and Research Grants No. DP200101792, No. DP210101900, No. DP210102831, No. DE220100462, No. LE210100098, and No. LE230100085; Austrian Federal Ministry of Education, Science and Research, Austrian Science Fund No. P 34529, No. J 4731, No. J 4625, and

No. M 3153, and Horizon 2020 ERC Starting Grant No. 947006 “InterLeptons”; Natural Sciences and Engineering Research Council of Canada, Compute Canada and CANARIE; National Key R&D Program of China under Contract No. 2022YFA1601903, National Natural Science Foundation of China and Research Grants No. 11575017, No. 11761141009, No. 11705209, No. 11975076, No. 12135005, No. 12150004, No. 12161141008, No. 12475093, and No. 12175041, China Postdoctoral Science Foundation GZC20240303 and 2024M760485, and Shandong Provincial Natural Science Foundation Project ZR2022JQ02; the Czech Science Foundation Grant No. 22-18469S and Charles University Grant Agency project No. 246122; European Research Council, Seventh Framework PIEF-GA-2013-622527, Horizon 2020 ERC-Advanced Grants No. 267104 and No. 884719, Horizon 2020 ERC-Consolidator Grant No. 819127, Horizon 2020 Marie Sklodowska-Curie Grant Agreement No. 700525 “NIOBE” and No. 101026516, and Horizon 2020 Marie Sklodowska-Curie RISE project JENNIFER2 Grant Agreement No. 822070 (European grants); L’Institut National de Physique Nucléaire et de Physique des Particules (IN2P3) du CNRS and L’Agence Nationale de la Recherche (ANR) under grant ANR-21-CE31-0009 (France); BMBF, DFG, HGF, MPG, and AvH Foundation (Germany); Department of Atomic Energy under Project Identification No. RTI 4002, Department of Science and Technology, and UPES SEED funding programs No. UPES/R&D-SEED-INFRA/17052023/01 and No. UPES/R&D-SOE/20062022/06 (India); Israel Science Foundation Grant No. 2476/17, U.S.-Israel Binational Science Foundation Grant No. 2016113, and Israel Ministry of Science Grant No. 3-16543; Istituto Nazionale di Fisica Nucleare and the Research Grants BELLE2, and the ICSC – Centro Nazionale di Ricerca in High Performance Computing, Big Data and Quantum Computing, funded by European Union – NextGenerationEU; Japan Society for the Promotion of Science, Grant-in-Aid for Scientific Research Grants No. 16H03968, No. 16H03993, No. 16H06492, No. 16K05323, No. 17H01133, No. 17H05405, No. 18K03621, No. 18H03710, No. 18H05226, No. 19H00682, No. 20H05850, No. 20H05858, No. 22H00144, No. 22K14056, No. 22K21347, No. 23H05433, No. 26220706, and No. 26400255, and the Ministry of Education, Culture, Sports, Science, and Technology (MEXT) of Japan; National Research Foundation (NRF) of Korea Grants No. 2016R1-D1A1B-02012900, No. 2018R1-A6A1A-06024970, No. 2021R1-A6A1A-03043957, No. 2021R1-F1A-1060423, No. 2021R1-F1A-1064008, No. 2022R1-A2C-1003993, No. 2022R1-A2C-1092335, No. RS-2023-00208693, No. RS-2024-00354342 and No. RS-2022-00197659, Radiation Science Research Institute, Foreign Large-Size Research Facility Application Supporting project, the Global Science Experimental Data Hub Center, the Korea Institute of Science and Technology Information (K24L2M1C4) and KREONET/GLORIAD; Universiti Malaya RU grant, Akademi Sains Malaysia, and Ministry of Education Malaysia; Frontiers of Science Program Contracts No. FOINS-296, No. CB-221329, No. CB-236394, No. CB-254409, and No. CB-180023, and SEP-CINVESTAV Research Grant No. 237 (Mexico); the Polish Ministry of Science and Higher Education and the National Science Center; the Ministry of Science and Higher Education of the Russian Federation and the HSE University Basic Research Program, Moscow; University of Tabuk Research Grants No. S-0256-1438 and No. S-0280-1439 (Saudi Arabia), and King Saud University,Riyadh, Researchers Supporting Project number (RSPD2024R873) (Saudi Arabia); Slovenian Research Agency and Research Grants No. J1-

9124 and No. P1-0135; Ikerbasque, Basque Foundation for Science, the State Agency for Research of the Spanish Ministry of Science and Innovation through Grant No. PID2022-136510NB-C33, Agencia Estatal de Investigacion, Spain Grant No. RYC2020-029875-I and Generalitat Valenciana, Spain Grant No. CIDEGENT/2018/020; the Swiss National Science Foundation; The Knut and Alice Wallenberg Foundation (Sweden), Contracts No. 2021.0174 and No. 2021.0299; National Science and Technology Council, and Ministry of Education (Taiwan); Thailand Center of Excellence in Physics; TUBITAK ULAKBIM (Turkey); National Research Foundation of Ukraine, Project No. 2020.02/0257, and Ministry of Education and Science of Ukraine; the U.S. National Science Foundation and Research Grants No. PHY-1913789 and No. PHY-2111604, and the U.S. Department of Energy and Research Awards No. DE-AC06-76RLO1830, No. DE-SC0007983, No. DE-SC0009824, No. DE-SC0009973, No. DE-SC0010007, No. DE-SC0010073, No. DE-SC0010118, No. DE-SC0010504, No. DE-SC0011784, No. DE-SC0012704, No. DE-SC0019230, No. DE-SC0021274, No. DE-SC0021616, No. DE-SC0022350, No. DE-SC0023470; and the Vietnam Academy of Science and Technology (VAST) under Grants No. NVCC.05.12/22-23 and No. DL0000.02/24-25.

These acknowledgements are not to be interpreted as an endorsement of any statement made by any of our institutes, funding agencies, governments, or their representatives.

We thank the SuperKEKB team for delivering high-luminosity collisions; the KEK cryogenics group for the efficient operation of the detector solenoid magnet and IBBelle on site; the KEK Computer Research Center for on-site computing support; the NII for SINET6 network support; and the raw-data centers hosted by BNL, DESY, GridKa, IN2P3, INFN, PNNL/EMSL, and the University of Victoria.

## References

[1] H. Y Cheng, *Charmed baryon physics circa 2021*, Chin. J. Phys. **78** (2022) 324-362.

[2] Particle Data Group, *The Review of Particle Physics*, Phys. Rev. D **110**, 030001 (2024).

[3] S. S. Tang, L. K. Li, X. Y. Zhou, and C. P. Shen, *Recent Measurements of Decay Asymmetry Parameter and CP Asymmetry for Charmed Baryon Decays at Belle* , Symmetry **15**, 91 (2023).

[4] Belle Collaboration, *Measurement of the Branching Fraction* $\Lambda_c^+ \to pK^-\pi^+$ , Phys. Rev. Lett. **113** (2014) 042002.

[5] BESIII Collaboration, *Measurements of Absolute Hadronic Branching Fractions of the* $\Lambda_c^+$ *Baryon* , Phys. Rev. Lett. **116** (2016) 052001.

[6] Belle Collaboration, *First Measurements of Absolute Branching Fractions of the* $\Xi_c^0$ *Baryon at Belle*, Phys. Rev. Lett. **122** (2019) 082001.

[7] Belle Collaboration, *First Measurements of Absolute Branching Fractions of the* $\Xi_c^+$ *Baryon at Belle*, Phys. Rev. D. **100** (2019) 031101(R).

[8] Belle and Belle II Collaboration, *Observations of the singly Cabibbo-suppressed decays* $\Xi_c^+ \to pK_S^0$, $\Xi_c^+ \to \Lambda\pi^+$, *and* $\Xi_c^+ \to \Sigma^0\pi^+$ *at Belle and Belle II*, arXiv:2412.10677.

[9] J. Q. Zou, F. R. Xu, G. B. Meng, and H. Y. Cheng, *Two-body hadronic weak decays of antitriplet charmed baryons*, Phys. Rev. D **101** (2020) 014011.

[10] C. Q. Geng, C. W. Liu, and T. H. Tsai, *Asymmetries of anti-triplet charmed baryon decays*, Phys. Lett. B **794** (2019) 19.

[11] H. J. Zhao, Y. L. Wang, Y. K. Hsiao, and Y. Yu, *A Diagrammatic Analysis of Two-Body Charmed Baryon Decays with Flavor Symmetry*, JHEP **02** (2020) 165.

[12] Y. K. Hsiao, Y. L. Wang, and H. J. Zhao, *Equivalent* $\mathrm{SU(3)_f}$ *approaches for two-body anti-triplet charmed baryon decays*, JHEP **09** (2022) 35.

[13] F. Huang, Z. P. Xing, and X. Z. He, *A global analysis of charmless two body hadronic decays for anti-triplet charmed baryons*, JHEP **03** (2022) 143.

[14] Z. P. Xing, X. Z. He, F. Huang, and C. Yang, *Global analysis of measured and unmeasured hadronic two-body weak decays of antitriplet charmed baryons*, Phys. Rev. D **108** (2023) 053004.

[15] C. W. Liu, *Nonleptonic two-body weak decays of charmed baryons*, Phys. Rev. D **109** (2024) 033004.

[16] H. Zhong, F. Xu, Q. Wen, and Y. Gu, *Weak decays of antitriplet charmed baryons from the perspective of flavor symmetry*, JHEP **02** (2023) 235.

[17] CLEO Collaboration, *Observation of new decay modes of the charmed-strange baryon* $\Xi_c^+$, Phys. Lett. B **373** (1996) 261.

[18] Belle Collaboration, *Physics achievements from the Belle experiment*, PTEP **2012** (2012) 04D001.

[19] Belle II Collaboration, *Measurement of the integrated luminosity of data samples collected during 2019-2022 by the Belle II experiment*, Chin. Phys. C **49** (2025) 013001.

[20] Belle Collaboration, *The Belle detector*, Nucl. Instr. and Methods Phys. Res. Sect. A **479** (2002) 117.

[21] Belle Collaboration, *Physics achievements from the Belle experiment*, Prog. Theor. Exp. Phys. **2012** (2012) 04D001.

[22] S. Kurokawa and E. Kikutani, *Overview of the KEKB accelerators*, Nucl. Instr. and Methods Phys. Res. Sect. A **499** (2003) 1, and other papers included in this volume.

[23] T. Abe *et al.*, *Achievements of KEKB*, Prog. Theor. Exp. Phys. **2013** (2013) 03A001, and references therein.

[24] Belle II Collaboration, *Belle II Technical Design Report*, arXiv:1011.0352.

[25] SuperKEKB Collaboration, *SuperKEKB Collider*, Nucl. Instr. and Methods Phys. Res. Sect. A **907** (2018) 188.

[26] T. Sjöstrand *et al.*, *High-energy physics event generation with PYTHIA 6.1*, Comput. Phys. Commun. **135** (2001) 238.

[27] T. Sjöstrand *et al.*, *An introduction to PYTHIA 8.2*, Comput. Phys. Commun. **191** (2015) 159.

[28] D. J. Lange, *The EvtGen particle decay simulation package*, Nucl. Instr. and Methods Phys. Res. Sect. A **462** (2001) 152.

[29] S. Jadach, B. F. L. Ward, and Z. Wąs, *The precision Monte Carlo event generator KK for two-fermion final states in $e^+e^-$ collisions*, Comput. Phys. Commun. **130** (2000) 260.

[30] E. Barberio and Z. Wąs, *PHOTOS: A Universal Monte Carlo for QED radiative corrections. Version 2.0*, Comput. Phys. Commun. **79** (1994) 291.

[31] R. Brun *et al.*, *GEANT3*, CERN Report No. DD/EE/84-1 (1984).

[32] GEANT4 collaboration, *GEANT4–a simulation toolkit*, Nucl. Instr. and Methods Phys. Res. Sect. A **506** (2003) 250.

[33] Belle II Framework Software Group, *The Belle II Core Software*, Comput. Softw. Big Sci. **3** (2019) 1.

[34] M. Gelb *et al.*, *B2BII: Data Conversion from Belle to Belle II*, Comput. Softw. Big Sci. **2** (2018) 9.

[35] E. Nakano, *Belle PID*, Nucl. Instr. and Methods Phys. Res. Sect. A **494** (2002) 402.

[36] Belle Collaboration, *Observation of an Excited $\Omega^-$ Baryon*, Phys. Rev. Lett. **121** (2018) 052003.

[37] Belle Collaboration, *Measurement of the resonant and nonresonant branching ratios in $\Xi_c^0 \to \Xi^0 K^+ K^-$*, Phys. Rev. D **103** (2021) 112002.

[38] Belle Collaboration, *Search for the semileptonic decays $\Xi_c^0 \to \Xi^0 \ell^+ \ell^-$ at Belle*, Phys. Rev. D **109** (2024) 052003.

[39] Belle Collaboration, *Measurements of the branching fractions of $\Xi_c^0 \to \Xi^0 \pi^0$, $\Xi_c^0 \to \Xi^0 \eta$, and $\Xi_c^0 \to \Xi^0 \eta'$ and asymmetry parameter of $\Xi_c^0 \to \Xi^0 \pi^0$*, JHEP **10** (2024) 045.

[40] M. Feindt and U. Kerzel, *The NeuroBayes neural network package*, Nucl. Instr. and Methods Phys. Res. Sect. A **559** (2006) 190.

[41] J.-F. Krohn *et al.*, *Global decay chain vertex fitting at Belle II*, Nucl. Instr. and Methods Phys. Res. Sect. A **976** (2020) 164269.

[42] X. Y. Zhou, S. X. Du, G. Li, and C. P. Shen, *TopoAna: A generic tool for the event type analysis of inclusive Monte-Carlo samples in high energy physics experiments*, Comput. Phys. Commun. **258** (2021) 107540.

[43] K. S. Cranmer, *Kernel estimation in high-energy physics*, Comput. Phys. Commun. **136** (2001) 198.

[44] S. S. Wilks, *The Large-Sample Distribution of the Likelihood Ratio for Testing Composite Hypotheses*, Ann. Math. Statist. **9** (1938) 60.

[45] G. D'Agostini, *On the use of the covariance matrix to fit correlated data*, Nucl. Instr. and Methods Phys. Res. Sect. A **346** (1994) 306.

[46] Belle II Collaboration, *The Belle II Physics Book*, Prog. Theor. Exp. Phys. **2019** (2019) 123C01; **2020** (2020) 029201(E).